

# Journal Pre-proof

Understanding synergistic catalysis on Pt-Cu diatomic sites via *operando* X-ray absorption spectroscopy in sulfur redox reactions

Shuai Xie, Xingjia Chen, Leilei Wang, Guikai Zhang, Haifeng Lv, Guolei Cai, Ying-Rui Lu, Ting-Shan Chan, Jing Zhang, Juncai Dong, Hongchang Jin, Xianghua Kong, Junling Lu, Song Jin, Xiaojun Wu, Hengxing Ji

PII: S2667-1417(23)00176-3

DOI: <https://doi.org/10.1016/j.esci.2023.100222>

Reference: ESCI 100222

To appear in: *eScience*

Received Date: 19 October 2023

Revised Date: 23 November 2023

Accepted Date: 29 November 2023

Please cite this article as: S. Xie, X. Chen, L. Wang, G. Zhang, H. Lv, G. Cai, Y.-R. Lu, T.-S. Chan, J. Zhang, J. Dong, H. Jin, X. Kong, J. Lu, S. Jin, X. Wu, H. Ji, Understanding synergistic catalysis on Pt-Cu diatomic sites via *operando* X-ray absorption spectroscopy in sulfur redox reactions, *eScience*, <https://doi.org/10.1016/j.esci.2023.100222>.

This is a PDF file of an article that has undergone enhancements after acceptance, such as the addition of a cover page and metadata, and formatting for readability, but it is not yet the definitive version of record. This version will undergo additional copyediting, typesetting and review before it is published in its final form, but we are providing this version to give early visibility of the article. Please note that, during the production process, errors may be discovered which could affect the content, and all legal disclaimers that apply to the journal pertain.

© 2023 The Authors. Published by Elsevier B.V. on behalf of Nankai University.



1 **Understanding synergistic catalysis on Pt-Cu diatomic sites**  
2 **via *operando* X-ray absorption spectroscopy in sulfur redox**  
3 **reactions**

4 Shuai Xie<sup>1†</sup>, Xingjia Chen<sup>2†</sup>, Leilei Wang<sup>3†</sup>, Guikai Zhang<sup>4</sup>, Haifeng Lv<sup>2</sup>, Guolei Cai<sup>1</sup>,  
5 Ying-Rui Lu<sup>5</sup>, Ting-Shan Chan<sup>5</sup>, Jing Zhang<sup>4</sup>, Juncai Dong<sup>4</sup>, Hongchang Jin<sup>1</sup>,  
6 Xianghua Kong<sup>6</sup>, Junling Lu<sup>3</sup>, Song Jin<sup>1\*</sup>, Xiaojun Wu<sup>2\*</sup>, Hengxing Ji<sup>1\*</sup>

7 <sup>1</sup>*Hefei National Laboratory for Physical Sciences at the Microscale, CAS Key*  
8 *Laboratory of Materials for Energy Conversion, Department of Applied Chemistry,*  
9 *University of Science and Technology of China, Hefei 230026.*

10 <sup>2</sup>*School of Chemistry and Material Sciences, CAS Key Laboratory of Materials for*  
11 *Energy Conversion, and CAS Center for Excellence in Nanoscience and Synergetic*  
12 *Innovation of Quantum Information and Quantum Technology, University of Science*  
13 *and Technology of China Hefei 230026.*

14 <sup>3</sup>*Hefei National Laboratory for Physical Sciences at the Microscale, Department of*  
15 *Chemical Physics, School of Chemistry and Materials Science, University of Science*  
16 *and Technology of China, Hefei 230026.*

17 <sup>4</sup>*Beijing Synchrotron Radiation Laboratory, Institute of High Energy Physics, Chinese*  
18 *Academy of Sciences, Beijing 100049.*

19 <sup>5</sup>*National Synchrotron Radiation Research Center, Hsinchu 300092.*

20 <sup>6</sup>*School of Chemistry and Chemical Engineering, Hefei University of Technology, Hefei*  
21 *230009.*

22

23 \*Corresponding author.

24 *E-mail:* js199155@ustc.edu.cn; xjwu@ustc.edu.cn; jihengx@ustc.edu.cn.

25

26 **Abstract**

27 Sulfur redox reactions render lithium–sulfur (Li–S) batteries with an energy density of >  
28 500 Wh kg<sup>-1</sup> but suffer a low practical capacity and fast capacity fade due to sluggish  
29 SRR kinetics, which lies in the complex reaction process that involves a series of  
30 reaction intermediates and proceeds via a cascade reaction. Here, we present a Pt-Cu  
31 dual-atom catalyst (Pt/Cu-NG) as an electrocatalyst for sulfur redox reactions. Pt/Cu-  
32 NG enabled the rapid conversion of soluble polysulfide intermediates into insoluble  
33 Li<sub>2</sub>S<sub>2</sub>/Li<sub>2</sub>S, and consequently, it prevented the accumulation and shuttling of lithium  
34 polysulfides, thus outperforming the corresponding single-atom catalysts (SACs) with  
35 individual Pt or Cu sites. *Operando* X-ray absorption spectroscopy and density

1 functional theory calculations revealed that a synergistic effect between the paired Pt  
2 and Cu atoms modifies the electronic structure of the Pt site through d-orbital  
3 interactions, resulting in an optimal moderate interaction of the metal atom with the  
4 different sulfide species. This optimal interaction enhanced charge transfer kinetics and  
5 promoted sulfur redox reactions. Our work thus provides important insights on the  
6 atomic scale into the synergistic effects operative in dual-atom catalysts and will thus  
7 pave the way to electrocatalysts with enhanced efficiency for high-performance Li-S  
8 batteries.

9 *Keywords:* Dual-atom catalysts, Sulfur redox reaction, Lithium-sulfur batteries,  
10 Synergistic interaction, X-ray absorption spectroscopy

## 12 **Introduction**

13 Lithium-sulfur (Li-S) batteries hold great promise for large-scale applications due  
14 to the compelling advantages of the cathode material sulfur, *viz.* its natural abundance,  
15 environmentally friendly nature, and high theoretical capacity ( $1675 \text{ mAh g}^{-1}$ ) [1,2].  
16 However, during the operation of a Li-S cell, the sulfur cathode undergoes a sluggish  
17 redox reaction process accompanied by multiphase transformation involving insoluble  
18  $\text{S}_8$ , soluble lithium polysulfides (LiPSs) and insoluble  $\text{Li}_2\text{S}_2/\text{Li}_2\text{S}$  [3]. This results in  
19 incomplete sulfur transformation, causing soluble LiPSs to accumulate in the  
20 electrolyte, which exacerbates the shuttle effect, leading to a low specific capacity of  
21 the cathode and a fast capacity fade [4-6]. Much effort has been dedicated to developing  
22 efficient electrocatalysts in the form of nanoparticles or as monodisperse single metal  
23 atoms (SACs) loaded on carbon substrates with the aim of promoting the kinetics of the  
24 redox reaction taking place at the sulfur cathode [7-10]. Electrocatalysts including  
25 metals, metal oxides, metal sulfides, and metal nitrides have been found to catalyze the

1 transformation of sulfur species.

2       The main challenge in developing electrocatalysts for Li–S batteries lies in  
3 promoting the complex sulfur conversion reaction. The sulfur redox reaction (SRR) is  
4 a cascade reaction starting with reactant  $S_8$ , followed by complex intermediates  $Li_2S_x$   
5 ( $x = 2, 4, 6, 8$ ) to finally form  $Li_2S$ . An effective catalyst can successfully provide active  
6 sites for the consecutive activation of a series of intermediates with complex molecular  
7 structures [11-14]. Hence, to accelerate the catalytic transformation, we need to design  
8 active binding sites that optimally balance the requirements of all steps in the catalytic  
9 cycle, especially at a low mass loading of the catalyst. SACs have a nearly 100% atom  
10 utilization efficiency, which allows a much lower mass loading than nanoparticles when  
11 used as a catalyst in Li–S batteries. However, the binding strength of polysulfides to a  
12 particular active metal site can be variable [15]. For example, the calculated binding  
13 energy of  $Li_2S_6$  on V-N<sub>4</sub>-C SAC is 3.37 eV, but it increased to 4.71 eV for  $Li_2S$  on the  
14 same metal active center [16]. The binding strength is also dependent on the type of  
15 SAC, e.g., the Fe-N<sub>4</sub>-C SAC exhibits a weaker adsorption towards both  $Li_2S_6$  (1.60 eV)  
16 and  $Li_2S$  (2.56 eV). Due to their relatively simple composition, conventional SACs  
17 provide little room for tuning the center metal atom-LiPS interaction to optimize its  
18 interaction with different LiPSs [17-19]. In contrast to SACs with totally isolated  
19 monoatomic sites, dual-atom catalysts have an additional interaction, namely, a  
20 metal–metal interaction, that gives the possibility of inducing synergistic effects  
21 through orbital interactions to allow electron transfer between adjacent paired metal  
22 atoms. Previous reports have shown that the electronic properties of dual-atom catalysts  
23 (DACs) can be favorably exploited towards SRR [20-22]. These effects have been  
24 mainly ascribed to a synergistic effect between the two adjacent metal centers that  
25 modifies catalytic behavior, even though the atomistic details of this effect remain

1 underexplored. This study was complicated by the multistep process in SRR, which  
2 requires *operando* structural analysis on electrocatalysts with precisely controlled  
3 structures.

4 Herein, we report a DAC consisting of Pt-Cu dual-atomic sites anchored on  
5 nitrogen-doped graphene (Pt/Cu-NG). Electrochemical measurements confirmed the  
6 superior catalytic activity of the Pt/Cu-NG catalytic system on the kinetics of sulfur  
7 redox reactions; the catalytic activity of our DAC system surpassed those of the SACs  
8 Pt-NG and Cu-NG, as well as a mixture of the two. The S@Pt/Cu-NG electrode (S mass  
9 ratio of 80 wt.%) exhibited a much higher electrochemical performance in a pouch cell.  
10 *Operando* X-ray absorption spectroscopy (XAS) and density functional theory (DFT)  
11 calculations indicate that the excellent electrocatalytic activity of the Pt/Cu-NG system  
12 originates from a synergistic effect between atomic Pt-Cu dual sites. The interatomic  
13 orbital interaction and charge transfer within paired Pt and Cu atoms effectively  
14 modulate the electronic structure of Pt, resulting in an optimal moderate interaction of  
15 the metal atom to the Li-S species. Our findings therefore provide a comprehensive  
16 understanding of the atomic-level phenomena in dual-atom catalysis. More specifically,  
17 using a combination of *operando* experiments and theory, we elucidate the synergistic  
18 effects present in double-atom active sites and their crucial role in improving the  
19 kinetics of sulfur redox reactions. We believe that such a comprehensive holistic  
20 understanding will provide a much-needed boost to designing efficient electrocatalysts  
21 for advanced Li-S batteries and enable their wide application.

## 22 **Material and methods**

23 **Synthesis of catalytic materials.** Cu-NG was prepared by pyrolysis of mixtures  
24 containing metal salts and graphene oxide (GO) powder under an NH<sub>3</sub> atmosphere.  
25 Nitrogen-doped graphene (NG) was prepared by the same method except that no metal

1 salt was added to the GO suspension. For more details, see Supplementary Text S1. The  
2 preparation of Pt/Cu-NG was carried out in a viscous atomic layer deposition (ALD)  
3 flow reactor (GEMSTAR-6 Benchtop ALD, Arradance) using  
4 trimethyl(methylcyclopentadienyl)-platinum (IV) ( $\text{MeCpPtMe}_3$ , 99%) and ultrahigh  
5 purity  $\text{O}_2$  (99.999%) as precursors with ultrahigh purity  $\text{N}_2$  (UHP, 99.999%) as the  
6 carrier gas at a flow rate of  $150 \text{ mL min}^{-1}$ . The Pt precursor was heated to  $65 \text{ }^\circ\text{C}$  to  
7 obtain a sufficiently high vapour pressure. The reactor inlets were held at  $100 \text{ }^\circ\text{C}$  to  
8 avoid any precursor condensation. Pt was deposited on Cu-NG at  $200 \text{ }^\circ\text{C}$  for one cycle.  
9 The timing sequence was 12, 180, 12, and 180 s for  $\text{MeCpPtMe}_3$  exposure,  $\text{N}_2$  purge,  
10  $\text{O}_2$  exposure, and  $\text{N}_2$  purge, respectively. Pt was deposited on NG using the same ALD  
11 procedure to prepare Pt/NG.

12 ***Operando* X-ray absorption spectroscopy measurements.** *Operando* XAS  
13 experiments were carried out using a homemade electrochemical cell. XAFS data were  
14 recorded at room temperature in fluorescence mode using a Lytle detector. The  
15 measured XAFS raw data were then background-subtracted, normalized and Fourier  
16 transformed in Athena. EXAFS fitting was performed for the FT  $k^2$ -weighted  
17 experimental EXAFS signals using Artemis software. Cu K-edge theoretical XANES  
18 calculations were carried out with FDMNES code in the framework of the real-space  
19 full multiple scattering (FMS) scheme using the muffin-tin approximation for the  
20 potential. With increasing temperature, the amplitude of the crystal lattice vibrations  
21 increases, leading to a broadening of the XANES spectra. We have taken into account  
22 the effect of temperature during the XANES simulation and the spectra convoluted  
23 using a Gaussian function to account for the broadening.

#### 24 **Theory/calculation**

25 First-principles calculations were performed based on *ab initio* DFT using the VASP

1 5.4.4 program. The generalized gradient approximation and Perdew–Burke–Ernzerhof  
2 exchange–correlation functional were adopted. A well-converged plane-wave cutoff of  
3 500 eV was used and the atomic coordinates were allowed to relax until the forces on  
4 the ions were less than  $0.03 \text{ eV } \text{\AA}^{-1}$ . The electronic convergence criterion was set to  $1$   
5  $\times 10^{-5} \text{ eV}$ . The reduced Brillouin zone was sampled with a  $\Gamma$ -centered  $2 \times 2 \times 1$  k-point  
6 mesh for optimization and a  $3 \times 3 \times 1$  k-point mesh for static calculations. A denser  $9$   
7  $\times 9 \times 1$  k-point mesh was used to calculate the density of states. A  $20 \text{ \AA}$  vacuum space  
8 was used in all the calculations to avoid interactions between the periodic images. The  
9 models for single/dual-atom catalysts were constructed using a  $7 \times 7$  supercell of  
10 graphene. Grimme D3 correction was used to describe the weak van der Waals  
11 interactions. The formation energies of Pt-Cu dual-atomic structures were calculated by  
12 the formula:  $E_{form} = E_{DAC} - E_{sub\_Cu} - E_{Pt}$ , where  $E_{DAC}$ ,  $E_{sub\_Cu}$ ,  $E_{Pt}$  represent  
13 energies of the considered dual-atomic structures, the corresponding Cu-NG substrates  
14 without Pt atom, a Pt atom in its bulk crystal, respectively. We selected the configuration  
15 with the most stable adsorption patterns from a variety of initial adsorption  
16 configurations as the optimal adsorption configuration for each adsorption structure.  
17 When calculating the formation energy of SACs or DACs with different structures, we  
18 adjusted the local coordination environment of metal atoms, including the types and  
19 positions of coordinating atoms, to finely control the bond lengths and bond angles  
20 between metals and coordinating atoms, thereby obtaining the least energetic structure.  
21 The adsorption energies ( $E_{ads}$ ) of  $S_8$  and several polysulfides on different surfaces were  
22 calculated by the following equation:  $E_{ads} = E_{total} - E_{sub} - E_{adsorbate}$ , where  
23  $E_{total}$ ,  $E_{sub}$  and  $E_{adsorbate}$  are energies of the adsorption configuration, the catalyst  
24 substrates, and isolated  $S_8$  and polysulfides molecules, respectively. The crystal orbital  
25 Hamilton population (COHP) analysis was performed with the LOBSTER 4.1.0

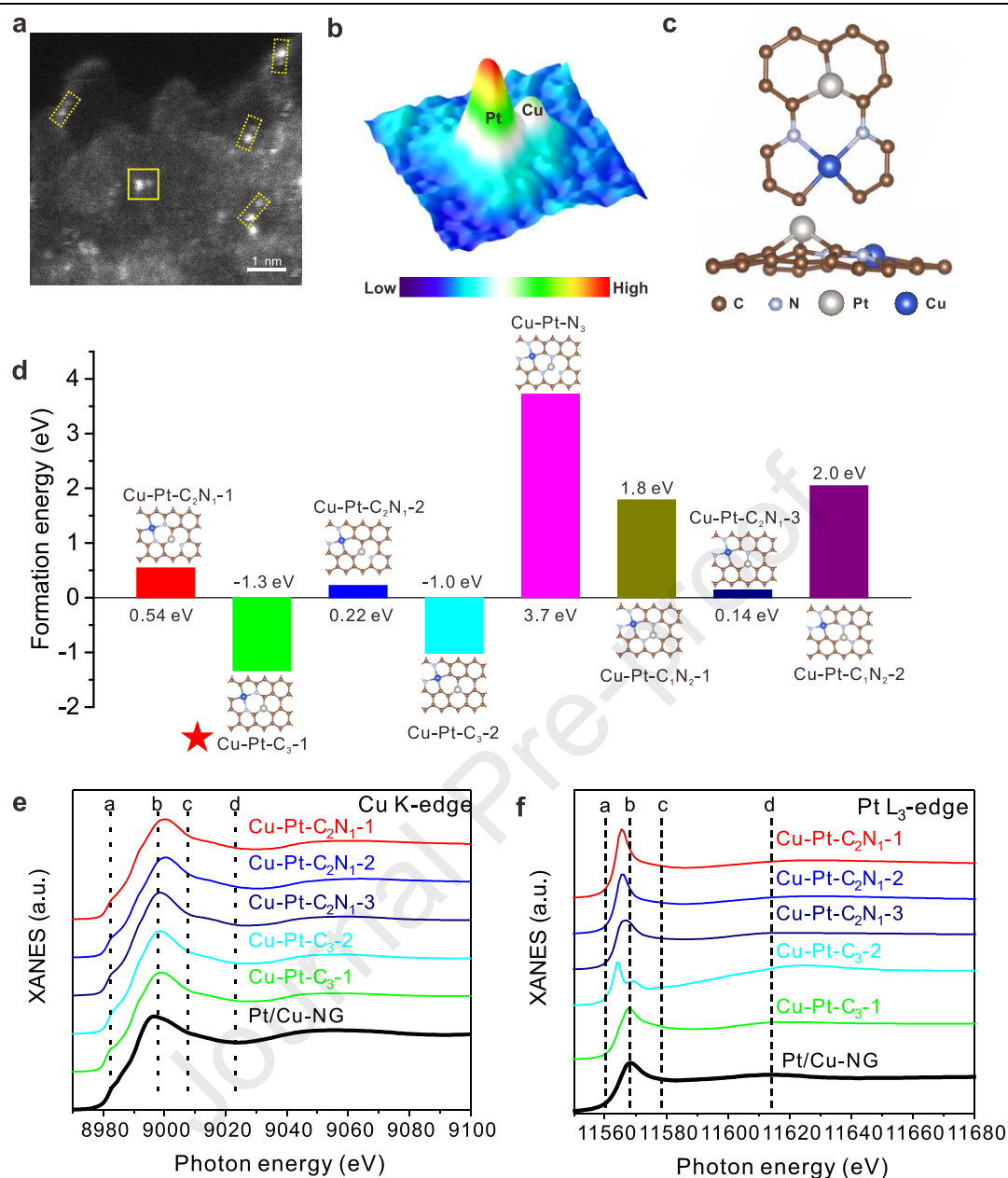
1 package. The barriers for  $\text{Li}_2\text{S}$  decomposition on catalysts were calculated with the  
2 climbing-image nudged elastic band (CI-NEB) method to evaluate de-lithiation  
3 reaction kinetics.

4 **Material characterization.** High-angle annular dark-field scanning transmission  
5 electron microscopy (HAADF-STEM) images were obtained by a JEOL JEM-  
6 ARF200F TEM/STEM instrument with a spherical aberration corrector operated at 200  
7 kV and 80 kV. TGA was carried out using a TA Q5000IR TGA under a flowing  $\text{N}_2$   
8 atmosphere with a heating rate of  $10\text{ }^\circ\text{C min}^{-1}$ . X-ray photoelectron spectroscopy (XPS)  
9 was performed on a Thermo ESCALAB 250Xi instrument with  $\text{Al K}\alpha$  radiation (1484.6  
10 eV) as the excitation source. Metal loading in the samples was determined by  
11 inductively coupled plasma-atomic emission spectroscopy (ICP–AES) using an Optima  
12 7300 DV spectrometer. X-ray powder diffraction patterns were acquired on a Rigaku  
13 X-ray diffractometer using  $\text{Cu-K}\alpha$  radiation as the X-ray source.

14 **Li–S cell assembly and electrochemical characterization.** See Supplementary Text  
15 S2.

16 **Results and discussion**





1

2 **Fig. 1. Synthesis and structural characterization of Pt-Cu diatomic sites.** (a) Aberration-

3 corrected HAADF-STEM image of Pt/Cu-NG. (b) 3D atom-overlapping Gaussian-function

4 fitting mappings of the area marked by the yellow square. (c) The most likely atomic

5 configuration for Pt/Cu-NG. (c) The formation energy of Pt-Cu dual-atomic structures when Pt

6 atoms are deposited on different substrates. The silver, blue, brown and light blue balls represent

7 Pt, Cu, C and N atoms, respectively. (e) Comparison of the experimental Cu K-edge XANES

8 spectrum of Pt/Cu-NG to the theoretical XANES spectrum. (f) Comparison of the experimental

9 Pt L<sub>3</sub>-edge XANES spectrum of Pt/Cu-NG to the theoretical XANES spectrum.

1 To demonstrate the synergistic effect of DACs that can effectively promote the  
2 sulfur redox reaction. Thus, the Cu and Pt atoms with little catalyzing effect are selected.  
3 The procedure to create Pt-Cu diatomic sites on nitrogen-doped graphene (Pt/Cu-NG)  
4 is presented in Figs. S1–S6 and in the Experimental Section. The aberration-corrected  
5 high-angle annular dark-field scanning transmission electron microscopy (HAADF-  
6 STEM) images show that Pt-Cu bimetallic sites can be well recognized by their  
7 different contrast due to their large difference in atomic number (Figs. 1a and 1b).  
8 Isolated single-Cu atoms (Cu-NG) and Pt single atoms (Pt-NG) on nitrogen-doped  
9 graphene were also prepared as the control samples (Figs. S2, S4, S5 and S6). The  
10 chemical states of Pt and Cu atoms in Pt/Cu-NG were identified by X-ray absorption  
11 spectroscopy (XAS). The oxidation state of Pt atoms in Pt-NG is calculated to be  
12 approximately +2.34, whereas it is +2.07 in Pt/Cu-NG (Figs. S7 and S8). However, the  
13 mean oxidation state of Cu atoms in Cu-NG is calculated to be +1.59, which is lower  
14 than that in Pt/Cu-NG (+1.67) (Figs. S9 and S10). The opposite trend in the change in  
15 the oxidation state of the Cu and Pt atoms in Pt/Cu-NG in comparison with Cu-NG and  
16 Pt-NG strongly demonstrates electronic interactions between the Pt and Cu atoms in  
17 Pt/Cu-NG, which is further confirmed by X-ray photoelectron spectroscopy (XPS, Fig.  
18 S11) and differential charge density analyses (Fig. S12). The Cu and Pt loadings in  
19 Pt/Cu-NG were determined to be ~0.36 and ~0.78 wt.%, respectively, by inductively  
20 coupled plasma-atomic emission spectroscopy (ICP–AES). This corresponds to a Cu/Pt  
21 atomic ratio of 1.4. Despite the fact that 28.5% of Cu atoms remain unutilized,  
22 increasing the cycle numbers of Pt ALD to enhance the content of Pt-Cu atomic pairs  
23 results in the observation of nanoparticles or clusters on the graphene sheets (Fig. S13).

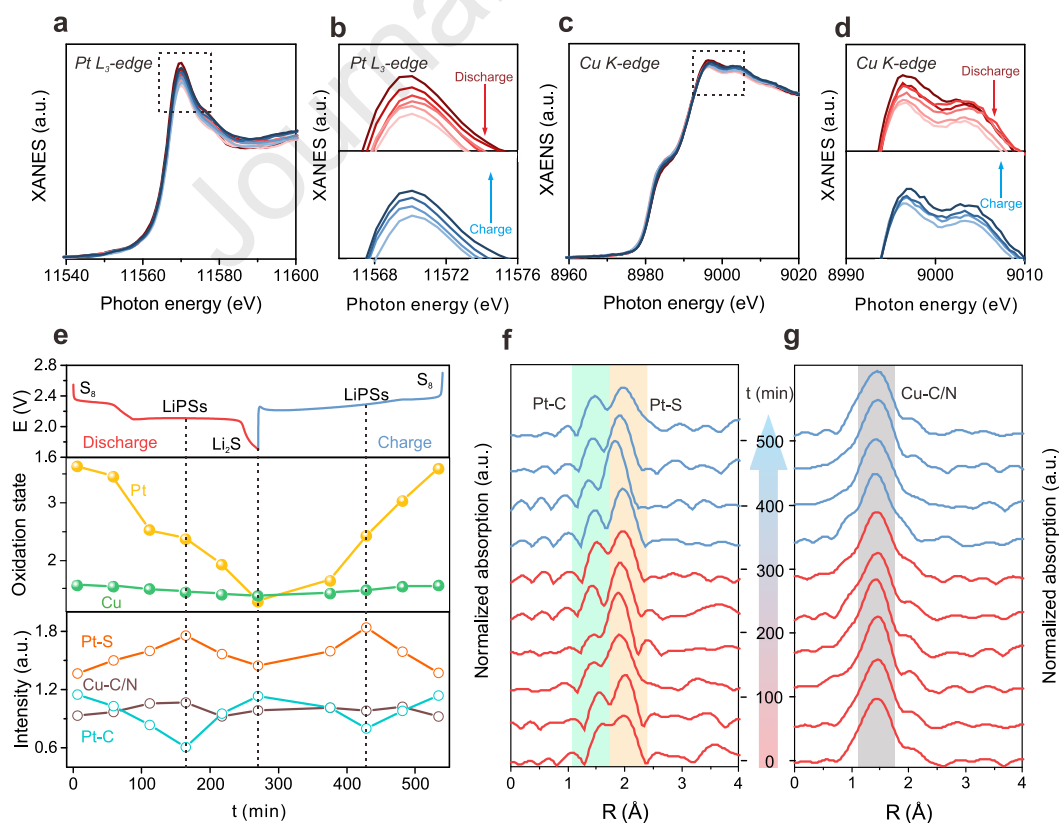
24 Unveiling the local structures of these catalysts is critical to understanding their  
25 synthesis mechanism and their catalytic applications. Through XAS and DFT analysis,

1 we successfully determined the most likely atomic configuration for Pt/Cu-NG, as  
2 depicted in Fig. 1c. The detailed process of structural analysis is outlined below. In our  
3 work, the Pt atoms in Pt/Cu-NG are introduced after the formation of Cu single sites.  
4 Therefore, we first investigated the local atomic coordination configuration of Cu-NG.  
5 The Fourier transform extended X-ray absorption fine structure (FT-EXAFS) spectra at  
6 the Cu K-edge are illustrated in Fig. S14. Cu-NG exhibits a main peak at 1.49 Å, which  
7 could be attributed to Cu-C/N coordination. Quantitative EXAFS curve fitting analysis  
8 gives a coordination number (CN) of four for Cu-NG, which we assign to Cu-C/N (Fig.  
9 S15a and Table S1). Considering the limit of EXAFS fitting in differentiating Cu-C and  
10 Cu-N coordination because of the close scattering amplitude of C and N, the  
11 coordination configurations of Cu may have seven types of structures by varying the  
12 number of C and N atoms, as shown in Fig. S16. To determine the most likely  
13 coordination structures of Cu atoms in Cu-NG, DFT calculations were performed based  
14 on the above proposed local coordination structures (Fig. S16). Five of them have a  
15 much lower formation energy of  $< -2.0$  eV, demonstrating that these structures are  
16 energetically favorable. Next, we continued our path toward resolving the atomic-site  
17 structure in Cu-NG by comparing the simulated XANES spectra with the experimental  
18 spectra. The results show that all simulated spectra are drastically different from the  
19 experimental spectra except Cu-C<sub>2</sub>N<sub>2</sub>-1 (Fig. S17). All the features for the experimental  
20 spectra are correctly reproduced for the Cu-C<sub>2</sub>N<sub>2</sub>-1 structure, especially for the weak  
21 preedge peak a and WL peak b. Together, these XANES simulations provide the solid  
22 spectroscopic fingerprint that a single Cu metal center presents in the form of Cu-C<sub>2</sub>N<sub>2</sub>-  
23 1 in the first coordination sphere, which is fully consistent with the EXAFS results.

24 After we confirmed the structure of Cu-NG, we investigated the EXAFS-wavelet  
25 transform (EXAFS-WT) spectra of Pt/Cu-NG at the Cu K-edge to determine that the

1 coordination structure of Cu is unchanged after introducing Pt atoms into Cu-NG.  
2 EXAFS-WT analyses of Cu-NG and Pt/Cu-NG show an identical intensity maximum  
3 at  $4.2 \text{ \AA}^{-1}$  (Fig. S18). The EXAFS fitting results further show that the coordination  
4 number of Cu-C/N paths in Pt/Cu-NG is estimated to be 4, confirming that the first  
5 coordination shell of Cu atoms is similar to that of Cu-NG (Fig. S15b and Table S1).  
6 Once we have determined the coordination configuration of the Cu atom in Pt/Cu-NG,  
7 the EXAFS spectrum of Pt/Cu-NG at the Pt  $L_3$ -edge is obtained to identify the local  
8 structure of the Pt atom. In the FT-EXAFS at the Pt  $L_3$  edge (Fig. S19), one prominent  
9 peak at  $1.55 \text{ \AA}$  assigned to Pt-C/N coordination is observed for Pt/Cu-NG. The  
10 coordination configurations for Pt/Cu-NG were then investigated by EXAFS curve-  
11 fitting analysis (Fig. S20). It is well fitted with a coordination number of Pt-C/N equal  
12 to three (Fig. S20b and Table S1). Therefore, we constructed a series of possible local  
13 coordination structures for the Pt-Cu diatomic site in the diatomic catalyst. In this case,  
14 the Cu atom is present in the coordinated form of  $\text{Cu-C}_2\text{N}_2\text{-1}$ , while the Pt atom is  
15 embedded in the graphene vacancy adjacent to the Cu site in the coordinated form of  
16  $\text{Pt-C}_x\text{N}_{3-x}$ . DFT predictions are performed based on the above proposed local  
17 coordination structures with changes in carbon or nitrogen (Fig. 1d). The formation  
18 energy is the lowest for the Pt-Cu dual-atomic structure when Pt atoms are inlaid in the  
19 graphene vacancy adjacent to the Cu sites via three C atoms, indicating that this  
20 structure is energetically the most favorable. To demonstrate the soundness of our  
21 proposed Pt-Cu atomic configuration, we perform structural refinement based on the  
22 five kinds of Pt-Cu dual-atomic structures that have relatively low formation energy as  
23 determined by DFT by simulating Cu K-edge and Pt  $L_3$ -edge XANES spectra. As  
24 shown in Figs. 1e and 1f, all the features from “a” to “d” in the experimental Cu K-  
25 edge and Pt  $L_3$ -edge XANES spectra of Pt/Cu-NG can be correctly reproduced, which

1 also convincingly validates the proposed structural model. We also followed a three-  
 2 step approach similar to that used for determining the structure of Cu-NG, and the  
 3 results demonstrate that Pt-C<sub>2</sub>N<sub>2</sub>-3 with N atoms at the crossing position is the most  
 4 likely structure for Pt-NG (Figs. S19–S22). To further investigate the stability of the  
 5 three catalysts, we performed *ab initio* molecular dynamics (AIMD) simulations (Fig.  
 6 S23). The AIMS simulations were performed for 5 ps with a time step of 1 fs with the  
 7 NVT ensemble using the Nosé–Hoover thermostat at 1100 K, 500 K, and 500 K for Cu-  
 8 NG, Pt-NG, and Pt/Cu-NG, respectively, according to their preparation temperature.  
 9 The structures remained intact without damage and bond breakage, which proved the  
 10 thermodynamic stability of the three selected structures and concluded that the catalyst  
 11 structures were reasonably optimized. In summary, the combination of EXAFS fitting,  
 12 DFT calculation and simulated XANES results unambiguously revealed the local  
 13 structure of Cu-NG, Pt-NG and Pt/Cu-NG.



14

15 **Fig. 2. Operando XAS characterization of Pt-Cu diatomic sites. Operando XANES**

1 spectra at the (a) Pt L<sub>3</sub>-edge and (c) Cu K-edge recorded for the whole Li-S  
2 electrochemical reaction process. (b) and (d) are the magnified white-line peaks of the  
3 XANES region. (e) Evolution of the electronic states and local coordination  
4 environment of Pt/Cu atoms during electrochemical cycling. Corresponding FT-  
5 EXAFS spectra at the (f) Pt L<sub>3</sub>-edge and (g) Cu K-edge.

6 Catalysts are expected to enhance the conversion process of sulfur species in Li-S  
7 batteries. To pinpoint the dynamic changes in the electronic state and local coordination  
8 environment of Pt and Cu atoms during this typical multistep reaction and their impact  
9 on catalytic performance, *operando* XAS was performed. The working Li-S cell was  
10 discharged to 1.7 V and charged back to 2.7 V. For the Pt L<sub>3</sub>-edge XANES (Figs. 2a  
11 and 2b), the WL intensity continues to decrease from OCV to 1.7 V and increases in the  
12 voltage range from 1.7 V to 2.7 V, pointing to a decrease in the number of unoccupied  
13 states of the Pt 5d orbital during discharge and an increase during charging. We note  
14 here that the WL intensity of the Cu K-edge XANES follows the same trend (Figs. 2c  
15 and 2d). This implies that the change in the electronic state of Cu atoms is reversible;  
16 this is also evidenced from the reversible shift of the absorption edge. These trends  
17 show that during the discharge/charge processes, charge transfer occurs in a reciprocal  
18 manner between the sulfur species and Pt/Cu atoms, leading to a reversible change in  
19 oxidation states. For a clearer comparison, we quantitatively estimated the average  
20 oxidation state of Pt and Cu atoms at different states based on the fitted XANES curves  
21 (Figs. S7–S10). Under OCV conditions, the oxidation state of Pt atoms increases to  
22 +3.65 compared to pristine Pt/Cu-NG, while that of Cu atoms decreases to +1.57,  
23 pointing to the effective adsorption of S<sub>8</sub> molecules over the Pt-Cu dual-atom sites (Fig.  
24 2e). Thus, when interacting with S<sub>8</sub> molecules, the oxidation states of Pt and Cu atoms  
25 change in the opposite direction with respect to their pristine counterpart, which in turn

1 is related to their different catalytic behavior. In the subsequent discharge process, the  
2 oxidation states of both Pt and Cu atoms decrease and nearly return to their initial states.  
3 The highly reversible electronic structure of Pt-Cu diatomic sites is the key to enhancing  
4 the catalytic activity for Li-S redox reactions. Notably, the Pt atoms undergo a more  
5 dramatic change in oxidation state during the cycling process than the Cu atoms, which  
6 we attribute to the stronger interaction of Pt with the sulfur species. It is thus the Pt  
7 atom rather than the Cu atom that is preferentially adsorbed and enables the conversion  
8 of sulfur species on the Pt-Cu diatomic site. The introduction of Cu offers the possibility  
9 to indirectly modulate the electronic structure of Pt to significantly increase the binding  
10 energies of the sulfur species and thereby enhance charge transfer between Pt and S.

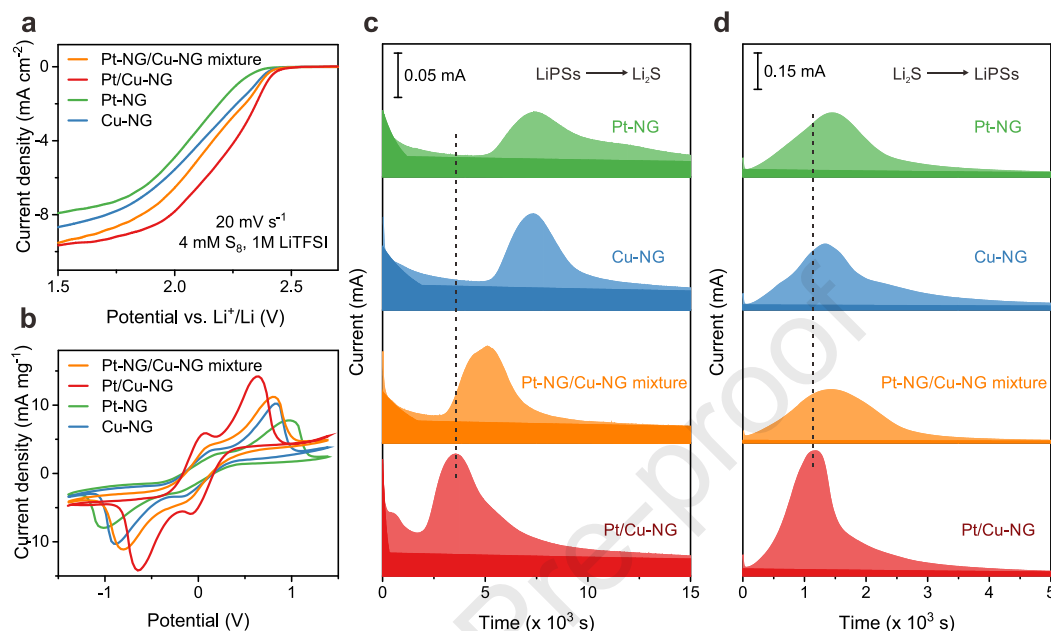
11 To probe the local structural evolution of the Pt-Cu dual-atom active sites occurring  
12 in situ, we performed *operando* FT-EXAFS at both Pt L<sub>3</sub>- and Cu K-edges. In the FT-  
13 EXAFS spectra at the Pt L<sub>3</sub>-edge (Fig. 2f), in addition to the original Pt-C/N  
14 coordination at 1.60 Å, a new peak appeared at approximately 1.98 Å when interacting  
15 with S<sub>8</sub> molecules at OCV, which remained present during the entire electrochemical  
16 reaction. XAS data from the literature indicate that this new signal from the Pt L<sub>3</sub>-edge  
17 could arise from Pt-S bonds [23,24]. In contrast, the FT-EXAFS spectra at the Cu K-  
18 edge only exhibit a single large peak derived from the Cu-C/N scattering path during  
19 the entire electrochemical cycling process (Fig. 2g). This difference strongly suggests  
20 that the Pt sites rather than the Cu sites preferentially interact with the sulfur species.  
21 We further monitored the variation in amplitude of the first coordination shell (below 2  
22 Å) of Pt and Cu atoms to reveal changes in the local coordination environment around  
23 the Pt-Cu diatomic sites (Fig. 2e). During the discharge process, an obvious increase in  
24 the Pt-S coordination amplitude can be seen as S<sub>8</sub> molecules are reduced to long chain  
25 lithium polysulfides. This peak reaches its maximum amplitude when discharged to the



1 middle of the second plateau. With further discharge to 1.7 V, the amplitude of the Pt-  
2 S peak significantly decreases, which we attribute to the reduced amount of polysulfides  
3 in the electrolyte due to their effective conversion to insoluble  $\text{Li}_2\text{S}_2/\text{Li}_2\text{S}$ . In the  
4 subsequent charging process, the intensity of the Pt-S peak increases with the  
5 appearance of polysulfides and returns to its original intensity at the end of the cycling  
6 process. Notably, the amplitude of the Pt-C/N coordination shows a totally opposite  
7 trend to the Pt-S coordination. This “trade-off” between the amplitudes of Pt-C/N and  
8 Pt-S peaks is testimony to the dynamic evolution of the Pt atomic sites due to their  
9 strong interaction with the sulfur species, in good agreement with the XANES results  
10 above. In stark contrast, the peak intensity corresponding to the Cu-C/N scattering path  
11 exhibits almost no change, pointing to the structural stability of the Cu atomic sites and  
12 their relatively weak interaction with the sulfur species. Taken together, the *operando*  
13 XAS results clearly demonstrate the presence of a synergistic effect in the Pt-Cu  
14 diatomic active sites. In fact, a reversible charge transfer process between the diatomic  
15 sites and the sulfur species can occur at both Pt and Cu atoms. More importantly, the  
16 more dynamic coordination structure of Pt atoms facilitates the adsorption of the sulfur  
17 species on the diatomic catalytic sites through a strong interaction. Simultaneously, Cu  
18 atoms, with a stable coordination structure, enable the effective desorption of the sulfur  
19 species off the diatomic catalytic sites by enabling effective charge distribution. Thus,  
20 the synergistic catalytic behavior of Pt and Cu atoms is the reason for the high catalytic  
21 efficiency of Pt-Cu diatomic sites, which greatly enhances the sulfur redox reaction  
22 kinetics. The electronic and geometric structures of carbon atoms could be adjustable  
23 by tailoring the central dopant atoms. This adjustment alters the absorption activity of  
24 reactants on metal atoms, thereby influencing their catalytic properties. Thus, the  
25 carbon atoms neighboring the dopant atoms may also significantly contribute to SRR.



1 However, the C K-edge XAS spectra of Pt-NG, Cu-NG, and Pt/Cu-NG exhibit minimal  
 2 differences, potentially due to the low proportion of carbon atoms that bind with metal  
 3 atoms (Fig. S24).



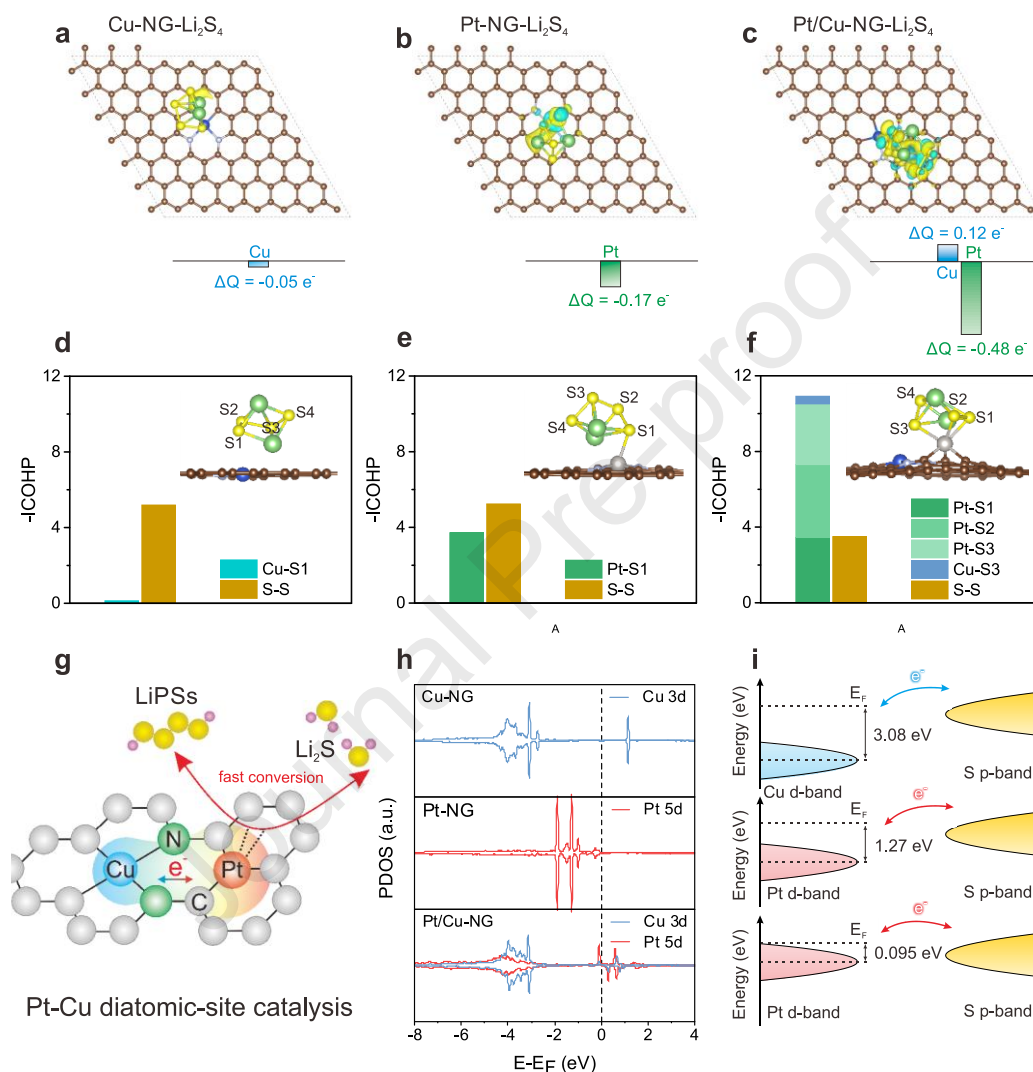
4  
 5 **Fig. 3. Kinetic behavior of sulfur redox reactions.** (a) LSV curves of Pt-NG, Cu-NG,  
 6 the Pt-NG/Cu-NG mixture and Pt/Cu-NG towards the sulfur reduction reaction. (b) CV  
 7 curves of Li<sub>2</sub>S<sub>6</sub> symmetrical cells with the Pt-NG, Cu-NG, Pt-NG/Cu-NG mixture and  
 8 Pt/Cu-NG electrodes. (c) Potentiostatic discharge profiles and (d) potentiostatic charge  
 9 profiles of the Pt-NG, Cu-NG, Pt-NG/Cu-NG mixture and Pt/Cu-NG electrodes.

10 We performed electrochemical studies on the Pt/Cu-NG and control samples,  
 11 including Pt-NG, Cu-NG, and a mixture of Pt-NG and Cu-NG prepared by hand  
 12 grinding Pt-NG and Cu-NG in a 1:1 mass ratio (Pt-NG/Cu-NG). We first performed  
 13 rotating disk electrode (RDE) measurements in a three-electrode cell using lithium foil  
 14 as the counter and reference electrodes and a glassy carbon electrode loaded with  
 15 catalyst as the working electrode. The electrolyte was 4 mM S<sub>8</sub> dissolved in 1 M LiTFSI  
 16 in a 1:1 (v/v) DOL/DME mixture. Fig. 3a shows the linear sweep voltammetry (LSV)  
 17 curves, where the onset potential and half-wave potential for Pt/Cu-NG are 2.47 V and

1 2.21 V, respectively, which are higher than those of the Pt-NG/Cu-NG mixture (2.44 V  
2 and 2.11 V), Cu-NG (2.43 V and 2.09 V) and Pt-NG (2.39 V and 2.06 V), suggesting  
3 enhanced kinetics of sulfur reduction when using Pt-Cu diatomic catalysts on NG. In  
4 addition, Pt/Cu-NG shows a minimum Tafel slope of 88 mV dec<sup>-1</sup> compared to the Pt-  
5 NG/Cu-NG mixture (98 mV dec<sup>-1</sup>), Cu-NG (100 mV dec<sup>-1</sup>) and Pt-NG (136 mV dec<sup>-1</sup>),  
6 demonstrating the intrinsically higher electrocatalytic activity of Pt/Cu-NG (Fig. S25).  
7 We calculated the number of electrons transferred during S<sub>8</sub> reduction based on the  
8 Koutecky-Levich equation (Fig. S26). In contrast to the control samples, the Pt/Cu-NG  
9 catalyst shows a higher electron transfer number (Fig. S27), suggesting that the  
10 presence of Pt-Cu diatomic sites leads to a more complete sulfur reduction reaction  
11 [25,26]. Next, we assembled Li<sub>2</sub>S<sub>6</sub> symmetric cells to further investigate the redox  
12 behavior of LiPSs on Pt-NG, Cu-NG, Pt-NG/Cu-NG mixtures and Pt/Cu-NG  
13 electrocatalysts. In all cases, the catalytic material was used as both the counter and the  
14 working electrode. Two pairs of reversible redox peaks are observed in all three cyclic  
15 voltammetry (CV) curves (Fig. 3b). Among the samples tested, Pt/Cu-NG exhibits the  
16 highest current response with distinct redox peaks, implying greater polysulfide  
17 conversion. Note that the CV profile of Pt/Cu-NG exhibits a much smaller separation  
18 between the reduction and oxidation peaks, demonstrating significantly improved  
19 reaction kinetics for polysulfide conversion [27]. The conversion of soluble LiPSs to  
20 Li<sub>2</sub>S contributes to as much as 75% of the theoretical capacity, and due to its sluggish  
21 kinetics, it is the rate-determining step [28]. To investigate the advantages of Pt/Cu-NG  
22 in promoting Li<sub>2</sub>S formation, we carried out potentiostatic discharge experiments using  
23 a Li<sub>2</sub>S<sub>8</sub> catholyte as the active sulfur species. As shown in the potentiostatic nucleation  
24 profiles (Fig. 3c), Pt/Cu-NG exhibits a higher current intensity at a lower response time  
25 than the Pt-NG, Cu-NG and Pt-NG/Cu-NG mixtures, suggesting rapid LiPS trapping

1 and deposition of  $\text{Li}_2\text{S}$  on the Pt/Cu-NG electrode. Moreover, the capacity of  $\text{Li}_2\text{S}$   
2 precipitation on Pt-Cu/NG ( $89 \text{ mAh g}^{-1}$ ) is higher than that of the Pt-NG/Cu-NG  
3 mixture ( $68 \text{ mAh g}^{-1}$ ), Cu-NG ( $65 \text{ mAh g}^{-1}$ ) and Pt-NG ( $56 \text{ mAh g}^{-1}$ ), confirming the  
4 enhanced kinetics of  $\text{Li}_2\text{S}$  deposition when using Pt-Cu/NG [29]. During charging, the  
5 sluggish oxidation kinetics of solid  $\text{Li}_2\text{S}$  are expected to hinder the reversibility of sulfur  
6 redox reactions. Therefore, we compared the reaction kinetics on the different catalytic  
7 materials by tracing the potentiostatic charge profiles to explore the oxidation behavior  
8 of  $\text{Li}_2\text{S}$  (Fig. 3d). Compared to the Pt-NG, Cu-NG and Pt-NG/Cu-NG mixtures, Pt/Cu-  
9 NG gave rise to a higher oxidation current peak in a shorter time, suggesting a  
10 significantly reduced energy barrier for  $\text{Li}_2\text{S}$  dissolution. Furthermore, the dissolution  
11 capacity of  $\text{Li}_2\text{S}$  estimated from the integral area under the potentiostatic charge curve  
12 was higher for Pt/Cu-NG than for the Pt-NG, Cu-NG and Pt-NG/Cu-NG mixtures,  
13 revealing effective oxidation of  $\text{Li}_2\text{S}$  on Pt/Cu-NG [30]. It is generally believed that  
14 carbon materials with a large specific surface area (SSA) could block LiPS diffusion in  
15 the cathode region through physical adsorption. To determine the SSA of Pt-NG, Cu-  
16 NG, and Pt/Cu-NG,  $\text{N}_2$  adsorption/desorption isotherms were obtained and are  
17 illustrated in Fig. S28. The SAA for Pt-NG, Cu-NG, and Pt/Cu-NG are measured at 101,  
18 83, and  $78 \text{ m}^2 \text{ g}^{-1}$ , respectively. To eliminate the influence of physical adsorption on  
19 catalytic behavior, an absorption test was conducted for Pt-NG, Cu-NG, and Pt/Cu-NG  
20 in a 3 mL 5 mM  $\text{Li}_2\text{S}_6$  solution in DOL/DME. The optical image and UV–Visible  
21 spectrophotometry (UV–Vis) results are depicted in Fig. S29. All three solutions  
22 exhibited a nearly identical color, lighter than the blank  $\text{Li}_2\text{S}_6$  solution. Furthermore,  
23 the UV–Vis curves for the three samples were analogous, indicating that LiPS  
24 absorption is similar on Pt-NG, Cu-NG, and Pt/Cu-NG. Consequently, the SSA in Pt-  
25 NG, Cu-NG, and Pt/Cu-NG does not significantly impact catalytic activity performance.

1 Taken together, these results point to the excellent electrocatalytic activity of Pt/Cu-NG  
 2 in regulating the kinetics of sulfur redox reactions. The results from control experiments  
 3 confirm that the Pt-Cu diatomic sites are responsible for the superior electrocatalytic  
 4 activity of Pt/Cu-NG due to the synergistic effect between the Pt/Cu atoms.



5

6 **Fig. 4. DFT calculations on the catalytic processes.** Differential charge density  
 7 distribution of  $\text{Li}_2\text{S}_4$  adsorbed on (a) Cu-NG, (b) Pt-NG, and (c) Pt/Cu-NG (yellow and  
 8 cyan stand for charge accumulation and depletion). The isosurface is  $0.003 \text{ e}/\text{bohr}^3$ .  
 9 Column charts in the lower panels represent the charge transfer number of Pt and Cu  
 10 atoms upon  $\text{Li}_2\text{S}_4$  adsorption. Crystal orbital Hamilton population (COHP) analysis of  
 11 metal-S bonds and S-S bonds for  $\text{Li}_2\text{S}_4$  adsorbed on (d) Cu-NG, (e) Pt-NG and (f)

- 1 Pt/Cu-NG. Insets are configuration models for the  $\text{Li}_2\text{S}_4$  adsorption system. (g)  
2 Schematic illustration of the proposed synergistic effect of Pt-Cu diatomic sites. (h)  
3 Projected density of states (PDOS) of metal atoms in Cu-NG, Pt-NG, and Pt/Cu-NG.  
4 (i) Schematic illustration of the  $d$ - $p$  orbital hybridized density of states.

5 To further understand the synergistic effect in the Pt-Cu diatomic active sites  
6 revealed by *operando* XAS results, we investigated the geometry and electronic  
7 structures of the metal active centers by DFT calculations (Figs. 4a–f). We used soluble  
8  $\text{Li}_2\text{S}_4$  as the representative sulfur species adsorbed on the metal active center for the  
9 following reasons: i) the electrochemical reaction of  $\text{Li}_2\text{S}_4$  transfers 1/3 of the total  
10 charge involved in the conversion reaction of the cathode, and ii) the binding strength  
11 of  $\text{Li}_2\text{S}_4$  is reported to be linearly correlated to the SRR overpotential [31]. We observed  
12 significant charge transfer between the Pt-Cu diatomic site and the  $\text{Li}_2\text{S}_4$  molecule with  
13 the charge accumulation/depletion region centered near the Pt atom (Fig. 4c and Table  
14 S2), which induced a massive change in the Pt charge number ( $0.48 e^-$ ) of the Pt-Cu  
15 site. This value is much higher than that of Cu ( $0.12 e^-$ ) in the Pt-Cu diatomic site and  
16 those of Pt ( $0.17 e^-$ ) and Cu ( $0.05 e^-$ ) in the SACs (Figs. 4a, 4b and Table S2), implying  
17 a strongly covalent bonding Pt-S bond [32]. The strengths of the Pt-S, Cu-S, and S–S  
18 bonds were further analysed by calculating the crystal orbital Hamilton population  
19 (COHP) and the integrated COHP (ICOHP) (Figs. 4d–f, S30 and S31). The Pt atom of  
20 Pt-NG and the Cu atom of Cu-NG bond to only the terminal S atom (S1) of  $\text{Li}_2\text{S}_4$ ,  
21 forming Pt-S1 and Cu-S1, respectively, with ICOHP values of  $-3.72$  and  $-0.13$  (Figs.  
22 4d and 4e). For Pt/Cu-NG, the Pt atom bonds to three S atoms, which are marked as Pt-  
23 S1, Pt-S2, and Pt-S3 with ICOHP values of  $-3.45$ ,  $-3.85$ , and  $-3.22$ , respectively,  
24 which are more negative than that of Cu-S3 ( $-0.40$ ) (Fig. 4f).

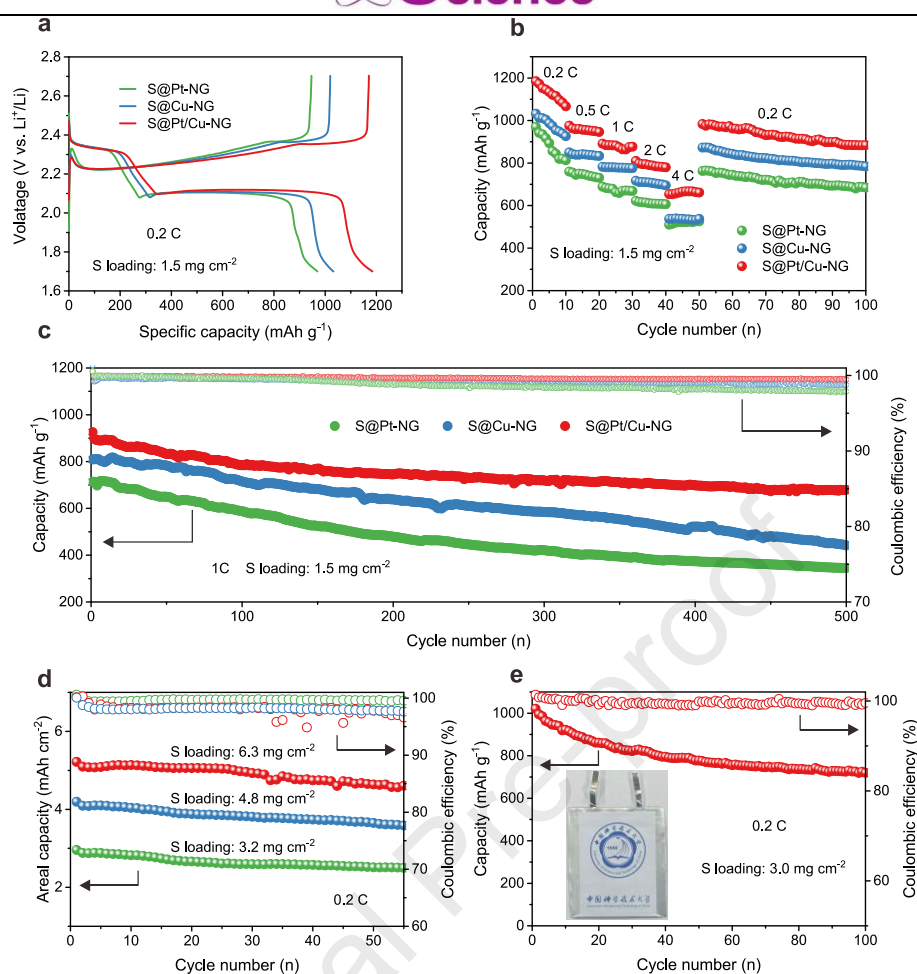
25 The more negative ICOHP values of Pt-S than Cu-S and the increased Pt-S bond

1 number in Pt/Cu-NG together indicate that the S species preferentially interact with the  
2 Pt atom, and this tendency is reinforced when a Cu atom is sitting next to Pt and S.  
3 Thus, the binding energies of the sulfur species (e.g., S<sub>8</sub>, Li<sub>2</sub>S<sub>4</sub>, and Li<sub>2</sub>S) are increased  
4 (Figs. S32 and S33) with an enhanced degree of charge transfer between Pt and S (Fig.  
5 4c). Considering the crucial role of solvation effects in modulating molecular structures  
6 and reaction behaviors in solutions, we incorporated an explicit solvation model (Fig.  
7 S34), which was compared to a vacuum model. Specifically, we allowed one or two  
8 1,2-dimethoxyethane (DME) molecules to interact with S<sub>8</sub>, Li<sub>2</sub>S<sub>4</sub>, and Li<sub>2</sub>S [33]. We  
9 found that the solvent effects on the configurations of the three catalysts and their DFT  
10 energy calculations were very small after considering solvation, and the trend of the  
11 magnitude of the adsorption energies remained unchanged (Fig. S35). These results are  
12 in very good accordance with the synergy effect as indicated by *operando* XAS analysis.

13 In the Pt-Cu diatomic site, the strong Pt-S bonding assisted by Cu leads to a much  
14 weaker S-S bond in Li<sub>2</sub>S<sub>4</sub>, as indicated by the COHP analysis (Figs. 4d-f). When Li<sub>2</sub>S<sub>4</sub>  
15 is attached to the Pt-Cu diatomic site, we observed a considerably greater occupation  
16 of the antibonding states for S-S than when Li<sub>2</sub>S<sub>4</sub> is attached to the Pt and Cu single  
17 metal atom sites (Fig. S31). In particular, the bonding states of S2-S3 of Li<sub>2</sub>S<sub>4</sub> on the  
18 Pt-Cu diatomic site are almost empty (or disappear, Fig. S31c). In comparison with Cu-  
19 NG and Pt-NG, the ICOHP values show a positive shift for Pt/Cu-NG, indicating  
20 weaker S-S binding when Li<sub>2</sub>S<sub>4</sub> is adsorbed on the Pt-Cu diatomic site (Figs. 4d-f).  
21 The weaker S-S bond facilitates the reversible cleavage and recombination of  
22 polysulfides with faster reaction kinetics during electrochemical reduction/oxidation  
23 reactions in the cathode of the Li-S battery. Furthermore, we evaluated the Li<sub>2</sub>S  
24 oxidation kinetics on different active sites by theoretical calculations (Fig. S36). The  
25 decomposition energy barrier of Li<sub>2</sub>S was significantly decreased for the Pt-Cu

1 diatomic site (0.64 eV) in contrast to that of the single Pt site (1.7 eV) and the Cu site  
2 (1.3 eV). The difference in the kinetics further proved the superiority of the Pt-Cu  
3 diatomic site. Single-atom catalysts containing Pt and Cu are found to be less active in  
4 catalyzing the sulfur redox reaction [34-36], which are more effective in demonstrating  
5 the effect of d-orbital electron coupling. The above synergistic effect in the Pt-Cu  
6 diatomic active sites unravelled by both *operando* XAS analysis (Fig. 2) and DFT  
7 calculations (Figs. 4a–4f) can be briefly summarized as follows. The presence of Cu  
8 adjacent to the Pt atom facilitates the formation of a Pt-S bond and enables charge  
9 transfer between the di-metal atom active site and sulfur species, which weakens the S–  
10 S bond and thereby accelerates sulfur redox reaction kinetics (Fig. 4g). This synergy  
11 originates essentially from the interaction between the d orbitals of Cu and Pt atoms,  
12 raising the d band center of Pt atoms close to the Fermi energy level, accompanied by  
13 a charge transfer from Cu to Pt atoms. The presence of highly populated and nearly  
14 continuous occupied and unoccupied states near the Fermi level (–0.095 eV) of Pt in  
15 Pt/Cu-NG (Figs. 4h and S37) is favorable for accepting/donating electrons from/to the  
16 sulfur species (Fig. 4i).





1

2 **Fig. 5. Electrochemical performance of Li-S cells based on different cathodes. (a)**

3 Galvanostatic discharge/charge profiles of cells with the S@Pt/Cu-NG cathode at 0.2

4 C. (b) Rate capability of S@Pt-NG, S@Cu-NG and S@Pt/Cu-NG cathodes from 0.2

5 C to 4 C. (c) Long-term cycling performance and Coulombic efficiencies of the cells

6 with S@Pt-NG, S@Cu-NG and S@Pt/Cu-NG cathodes at 1 C. (d) Cycling performance

7 of S@Pt/Cu-NG cathodes with high sulfur loading at 0.2 C. (e) Cycling performance

8 of the Li-S pouch cell with Pt/Cu-NG as the cathode catalyst.

9 In view of the superior electrocatalytic activity of Pt-Cu dual sites towards SRR,

10 we applied the S@Pt-NG, S@Cu-NG and S@Pt/Cu-NG composites as cathodes in

11 Li-S full cells. The sulfur content was measured to be ~ 80 wt.% (Fig. S38). Fig. 5a

12 shows the galvanostatic discharge/charge profiles of the electrodes with an S mass

13 loading of 1.5 mg cm<sup>-2</sup>. The S@Pt/Cu-NG electrode delivers an initial discharge



1 capacity of 1185 mAh g<sup>-1</sup> at 0.2 C, which is higher than that for S@Pt-NG (970 mAh  
2 g<sup>-1</sup>) and S@Cu-NG (1033 mAh g<sup>-1</sup>). At higher rates of 0.5 C, 1 C, 2 C and 4 C, the  
3 S@Pt/Cu-NG electrode shows satisfactory performance, with capacities of 976 mAh  
4 g<sup>-1</sup>, 891 mAh g<sup>-1</sup>, 810 mAh g<sup>-1</sup> and 667 mAh g<sup>-1</sup>, respectively (Fig. 5b). These values  
5 are considerably higher than those observed for the control samples, indicating the  
6 improved rate capability of S@Pt/Cu-NG. Furthermore, the acceleration of SRR  
7 promotes the transformation of dissolved LiPSs and thereby suppresses the shuttle  
8 effect, leading to improved cycling stability. The S@Pt/Cu-NG electrode exhibits a  
9 higher capacity retention rate of 83% after 100 cycles at 0.2 C (Fig. S39), compared to  
10 the S@Pt-NG (72%) and S@Cu-NG electrodes (74%). Long-term cycling stability tests  
11 were further carried out at 1 C, as shown in Fig. 5c. The S@Pt/Cu-NG electrode delivers  
12 a specific capacity of 680 mAh g<sup>-1</sup> after 500 cycles with a capacity decay of 0.053%  
13 per cycle and a Coulombic efficiency of 99.5%. To assess the stability of Pt/Cu-NG, we  
14 conducted HAADF-STEM to confirm the dispersed state of Pt-Cu dual-atomic sites  
15 after 500 discharge–charge cycles under 1C. The HAADF-STEM image (Fig. S40)  
16 illustrates that the Pt/Cu-NG species remain uniformly dispersed, with no discernible  
17 metal-related nanoparticles. This observation underscores the long-term stability of  
18 Pt/Cu-NG. In contrast, the specific capacity of the S@Pt-NG and S@Cu-NG electrodes  
19 declined progressively to only 345 mAh g<sup>-1</sup> (capacity degradation rate of 0.10% and  
20 Coulombic efficiency of 97.9%) and 442 mAh g<sup>-1</sup> (capacity degradation rate of 0.091%  
21 and Coulombic efficiency of 98.7%), respectively. The cycling performances of the  
22 S@Pt/Cu-NG electrode with high sulfur loadings of 3.2, 4.8, and 6.3 mg cm<sup>-2</sup> were  
23 evaluated (Fig. 5d). Notably, the electrodes with high sulfur loadings of 6.3 mg cm<sup>-2</sup>  
24 still delivered an initial areal capacity of 5.2 mAh cm<sup>-2</sup>. We also fabricated a Li–S  
25 pouch cell based on an S@Pt/Cu-NG cathode with a sulfur loading of 3.0 mg cm<sup>-2</sup>,

1 which delivered an initial discharge capacity of 1021 mAh g<sup>-1</sup> corresponding to an areal  
2 capacity of 3.0 mAh cm<sup>-2</sup> and a reversible capacity of 720 mAh g<sup>-1</sup> after 100 cycles at  
3 0.2 C (Figs. 5e and S41), demonstrating the suitability of Pt-Cu DACs at practical sulfur  
4 loadings used in a working battery. A “Pt-Cu”-shaped light-emitting diode (LED) array  
5 with 88 bulbs could be powered by the assembled pouch cell when folded or bent in  
6 different ways, showing the application potential of the S@Pt/Cu-NG electrode in  
7 flexible Li-S batteries (Fig. S41).

## 8 **Conclusions**

9 In summary, we successfully created atomically dispersed Pt-Cu diatomic active  
10 sites on nitrogen-doped graphene. The Pt-Cu diatomic sites were found to be highly  
11 efficient electrocatalysts for multiphase sulfur redox reactions, outperforming single-  
12 atom Cu and Pt sites. The combination of *operando* XAS analysis and DFT calculations  
13 revealed a synergistic effect in the Pt-Cu dual-atom catalytic sites, arising from the  
14 modulated density of states of the Pt atom by the adjacent Cu. This facilitates the  
15 formation of the Pt-S bond and charge transfer between the di-metal atom active site  
16 and sulfur species. As a result, the S-S bond is weakened, resulting in accelerated sulfur  
17 redox reaction kinetics. When applied in working Li-S coin cells, the S@Pt/Cu-NG  
18 electrode enabled a stable long-term cycling performance with a small capacity fading  
19 of 0.053% per cycle after 500 cycles at 1 C and a high areal capacity of 5.2 mAh cm<sup>-2</sup>  
20 at high sulfur loading (6.3 mg cm<sup>-2</sup>) at 0.2 C, demonstrating great potential for practical  
21 application. Our findings therefore provide insight at the atomic level in dual-atom  
22 catalysis and shed light on synergistic effects present in double-atom active sites that  
23 play a crucial role in improving the kinetics of sulfur redox reactions.

24

## 25 **Author contributions**

1 H.J., S.J. and S.X. conceived and designed the experimental research. X.S., L.W.  
2 and J.L. performed the catalyst synthesis and structural characterization. X.C., H.L. and  
3 X.W. designed and performed the DFT calculations. S.X. performed the  
4 electrochemical measurements with the assistance of G.C. and conducted the data  
5 analysis with contributions from H.J. and X.K. G.Z., J.Z., J.D., Y.-R.L. and T.-S.C.  
6 contributed to synchrotron X-ray measurements and analysis. S.X., S.J., X.W. and H.J.  
7 wrote and revised the manuscript. All authors discussed the results and commented on  
8 the manuscript. S.X., X.C. and L.W. contributed equally to this work.

9

### 10 **Competing financial interests**

11 The authors declare no competing financial interests.

12

### 13 **Acknowledgements**

14 This work was supported by the Natural Science Foundation of China (22125902,  
15 21975243, U2032202, and U1932201), the National Program for Support of Topnotch  
16 Young Professionals, the DNL Cooperation Fund, CAS (DNL202020), the Anhui  
17 Science Fund for Distinguished Young Scholars (2208085J15), the National Key R&D  
18 Program of China (No. 2022YFA1504101) and Users with Excellence Program of  
19 Hefei Science Center CAS (2021HSC-UE002).

20

### 21 **References**

22 [1] Y. Li, S. Guo, Material design and structure optimization for rechargeable lithium-  
23 sulfur batteries, *Matter* 4 (2021) 1142-1188.

24 [2] Y. Chen, T. Wang, H. Tian, D. Su, Q. Zhang, G. Wang, Advances in lithium-sulfur  
25 batteries: from academic research to commercial viability, *Adv. Mater.* 33 (2021)

1 2003666.

2 [3] S.-F. Ng, M. Y. L. Lau, W.-J. Ong, Lithium-sulfur battery cathode design: tailoring  
3 metal-based nanostructures for robust polysulfide adsorption and catalytic conversion,  
4 *Adv. Mater.* 33 (2021) 2008654.

5 [4] J. Liang, Z.-H. Sun, F. Li, H.-M. Cheng, Carbon materials for Li-S batteries:  
6 functional evolution and performance improvement, *Energy Storage Mater.* 2 (2016)  
7 76-106.

8 [5] Z. W. Seh, Y. Sun, Q. Zhang, Y. Cui, Designing high-energy lithium-sulfur batteries,  
9 *Chem. Soc. Rev.* 45 (2016) 5605-5634.

10 [6] Y. V. Mikhaylik, J. R. Akridge, Polysulfide shuttle study in the Li/S battery system,  
11 *J. Electrochem. Soc.* 151 (2004) A1969.

12 [7] H. Ye, J. Y. Lee, Solid additives for improving the performance of sulfur cathodes  
13 in lithium-sulfur batteries-adsorbents, mediators, and catalysts, *Small Methods* 4 (2020)  
14 1900864.

15 [8] P. Wang, B. Xi, M. Huang, W. Chen, J. Feng, S. Xiong, Emerging catalysts to  
16 promote kinetics of lithium-sulfur batteries, *Adv. Energy Mater.* 11 (2021) 2002893.

17 [9] Z. Liang, J. Shen, X. Xu, F. Li, J. Liu, B. Yuan, Y. Yu, M. Zhu, Advances in the  
18 development of single-atom catalysts for high-energy-density lithium-sulfur batteries.  
19 *Adv. Mater.* 34 (2022) 2200102.

20 [10] F. Wang, J. Li, J. Zhao, Y. Yang, C. Su, Y. L. Zhong, Q.-H. Yang, J. Lu, Single-  
21 atom electrocatalysts for lithium sulfur batteries: progress, opportunities, and  
22 challenges, *ACS Mater. Lett.* 2 (2020) 1450-1463.

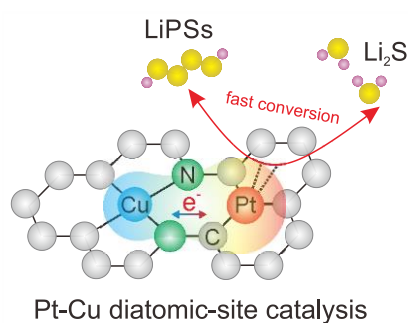
- 1 [11] M. Vijayakumar, N. Govind, E. Walter, S. D. Burton, A. Shukla, A. Devaraj, J.  
2 Xiao, J. Liu, C. Wang, A. Karim, S. Thevuthasan, Molecular structure and stability of  
3 dissolved lithium polysulfide species, *Physics Phys. Chem. Chem. Phys.* 16 (2014)  
4 10923-10932.
- 5 [12] T. Zhang, L. Zhang, Y. Hou, MXenes: synthesis strategies and lithium-sulfur  
6 battery applications, *eScience* 2 (2022)164-182.
- 7 [13] Z. Shen, X. Jin, J. Tian, M. Li, Y. Yuan, S. Zhang, S. Fang, X. Fan, W. Xu, H. Lu,  
8 J. Lu, H. Zhang, Cation-doped ZnS catalysts for polysulfide conversion in lithium-  
9 sulfur batteries, *Nat. Catal.* 5 (2022) 555-563.
- 10 [14] S. Xie, X. Chen, C. Wang, Y.-R. Lu, T.-S. Chan, C.-H. Chuang, J. Zhang, W. Yan,  
11 S. Jin, H. Jin, X. Wu, H. Ji, Role of the metal atom in a carbon-based single-atom  
12 electrocatalyst for Li-S redox reactions, *Small* 18 (2022) 2200395.
- 13 [15] Q.-W. Zeng, R.-M. Hu, Z.-B. Chen, J.-X. Shang, Single-atom Fe and N co-doped  
14 graphene for lithium-sulfur batteries: a density functional theory study, *Mater. Res.*  
15 *Express* 6 (2019) 095620.
- 16 [16] E. I. Andritsos, C. Lekakou, Q. Cai, Single-atom catalysts as promising cathode  
17 materials for lithium-sulfur batteries, *J. Phys. Chem. C* 125 (2021) 18108-18118.
- 18 [17] L. Ma, J. Qian, Y. Li, Y. Cheng, S. Wang, Z. Wang, C. Peng, K. Wu, J. Xu, I. Manke,  
19 C. Yang, P. Adelhelm, R. Chen, Binary metal single atom electrocatalysts with  
20 synergistic catalytic activity toward high-rate and high areal-capacity lithium-sulfur  
21 batteries, *Adv. Funct. Mater.* 32 (2022) 2208666.
- 22 [18] Y. Feng, L. Zu, S. Yang, L. Chen, K. Liao, S. Meng, C. Zhang, J. Yang, Ultrahigh-

- 1 content Co-P cluster as a dual-atom-site electrocatalyst for accelerating polysulfides  
2 conversion in Li-S batteries, *Adv. Funct. Mater.* 32 (2022) 2207579.
- 3 [19] Z. Du, X. Chen, W. Hu, C. Chuang, S. Xie, A. Hu, W. Yan, X. Kong, X. Wu, H. Ji,  
4 L.-J. Wan, Cobalt in nitrogen-doped graphene as single-atom catalyst for high-sulfur  
5 content lithium-sulfur batteries, *J. Am. Chem. Soc.* 141 (2019) 3977-3985.
- 6 [20] L. Shen, Y.-W. Song, J. Wang, C.-X. Zhao, C.-X. Bi, S.-Y. Sun, X.-Q. Zhang, B.-  
7 Q. Li, Q. Zhang, Synergistic catalysis on dual-atom sites for high-performance lithium-  
8 sulfur batteries, *Small Struct.* 4 (2023) 2200205.
- 9 [21] X. Sun, Y. Qiu, B. Jiang, Z. Chen, C. Zhao, H. Zhou, L. Yang, L. Fan, Y. Zhang,  
10 N. Zhang, Isolated Fe-Co heteronuclear diatomic sites as efficient bifunctional catalysts  
11 for high-performance lithium-sulfur batteries, *Nat. Commun.* 14 (2023) 291.
- 12 [22] C. Dong, C. Zhou, M. Wu, Y. Yu, K. Yu, K. Yan, C. Shen, J. Gu, M. Yan, C. Sun,  
13 L. Mai, X. Xu, Boosting bi-directional redox of sulfur with dual metal single atom pairs  
14 in carbon spheres toward high-rate and long-cycling lithium-sulfur battery, *Adv. Energy*  
15 *Mater.* 13 (2023) 2301505.
- 16 [23] L. Wang, M.-X. Chen, Q.-Q. Yan, S.-L. Xu, S.-Q. Chu, P. Chen, Y. Lin, H.-W.  
17 Liang, A sulfur-tethering synthesis strategy toward high-loading atomically dispersed  
18 noble metal catalysts, *Sci. Adv.* 5 (2019) eaax6322.
- 19 [24] Q.-Q. Yan, D.-X. Wu, S.-Q. Chu, Z.-Q. Chen, Y. Lin, M.-X. Chen, J. Zhang, X.-J.  
20 Wu, H.-W. Liang, Reversing the charge transfer between platinum and sulfur-doped  
21 carbon support for electrocatalytic hydrogen evolution, *Nat. Commun.* 10 (2019) 4977.
- 22 [25] Y.-C. Lu, Q. He, H. A. Gasteiger, Probing the lithium-sulfur redox reactions: A

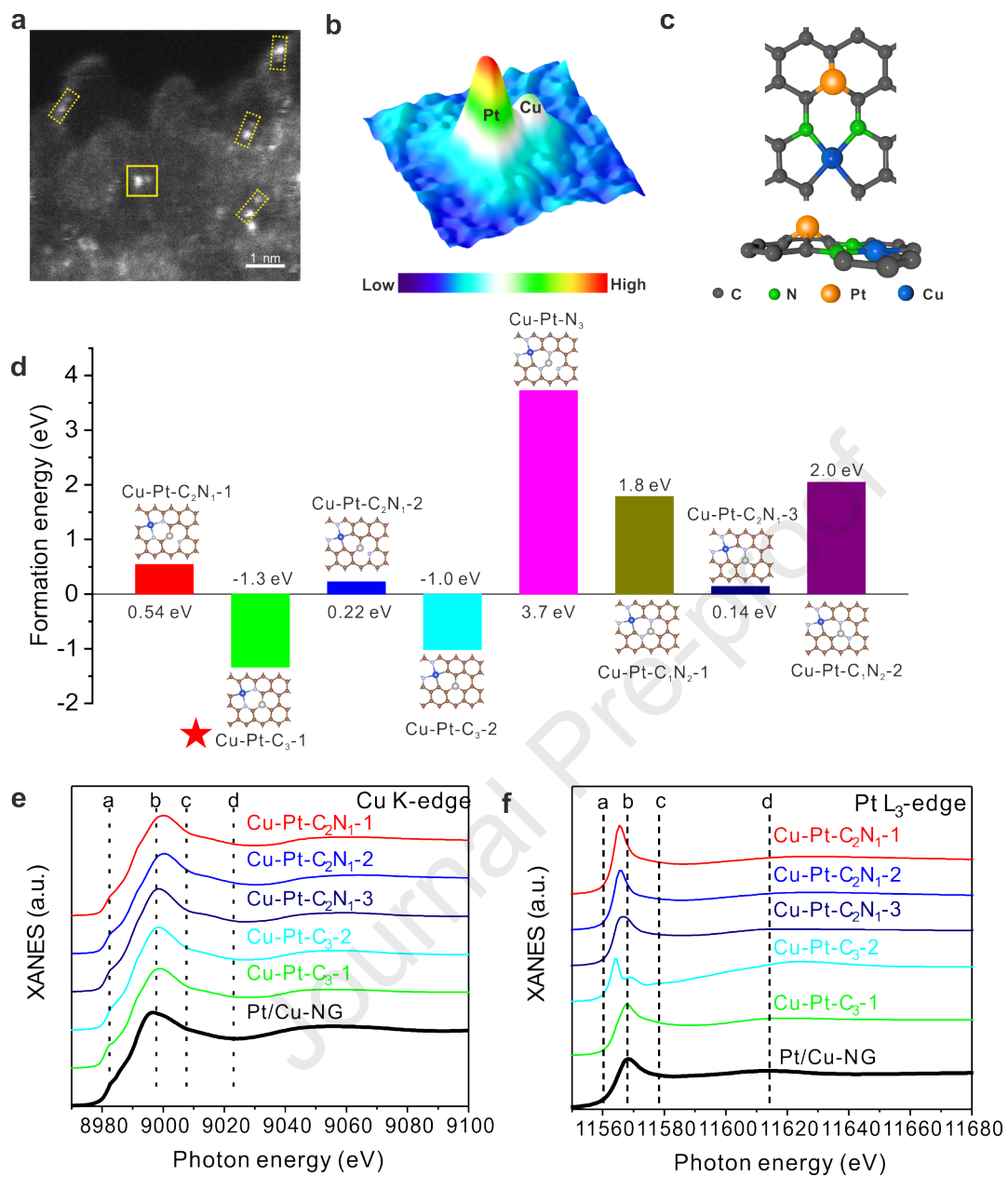
- 1 rotating-ring disk electrode study, *J. Phys. Chem. C* 118 (2014) 5733-5741.
- 2 [26] L. Peng, Z. Wei, C. Wan, J. Li, Z. Chen, D. Zhu, D. Baumann, H. Liu, C. S. Allen,  
3 X. Xu, A. I. Kirkland, I. Shakir, Z. Almutairi, S. Tolbert, B. Dunn, Y. Huang, P. Sautet,  
4 X. Duan, A fundamental look at electrocatalytic sulfur reduction reaction, *Nat. Catal.* 3  
5 (2020) 762-770.
- 6 [27] H. Lin, L. Yang, X. Jiang, G. Li, T. Zhang, Q. Yao, G. W. Zheng, J. Y. Lee,  
7 Electrocatalysis of polysulfide conversion by sulfur-deficient MoS<sub>2</sub> nanoflakes for  
8 lithium-sulfur batteries, *Energy Environ. Sci.* 10 (2017) 1476-1486.
- 9 [28] W.-G. Lim, S. Kim, C. Jo, J. Lee, Comprehensive review of materials with catalytic  
10 effects in Li-S batteries: enhanced redox kinetics, *Angew. Chem. Int. Ed.* 58 (2019)  
11 18746-18757.
- 12 [29] F. Y. Fan, W. C. Carter, Y.-M. Chiang, Mechanism and kinetics of Li<sub>2</sub>S precipitation  
13 in lithium-sulfur batteries, *Adv. Mater.* 27 (2015) 5203-5209.
- 14 [30] R. Wang, C. Luo, T. Wang, G. Zhou, Y. Deng, Y. He, Q. Zhang, F. Kang, W. Lv,  
15 Q.-H. Yang, Bidirectional catalysts for liquid-solid redox conversion in lithium-sulfur  
16 batteries, *Adv. Mater.* 32 (2020) 2000315.
- 17 [31] L. Wang, Z. Hu, X. Wan, W. Hua, H. Li, Q.-H. Yang, W. Wang, Li<sub>2</sub>S<sub>4</sub> Anchoring  
18 governs the catalytic sulfur reduction on defective SmMn<sub>2</sub>O<sub>5</sub> in lithium-sulfur battery,  
19 *Adv. Energy Mater.* 12 (2022) 2200340.
- 20 [32] S. Sun, X. Zhang, S. Wang, First-principles investigation on the bonding  
21 mechanism between graphyne and the (111) surface of Cu, Ag and Au, *Mater. Res.*  
22 *Express* 7 (2020) 065603.

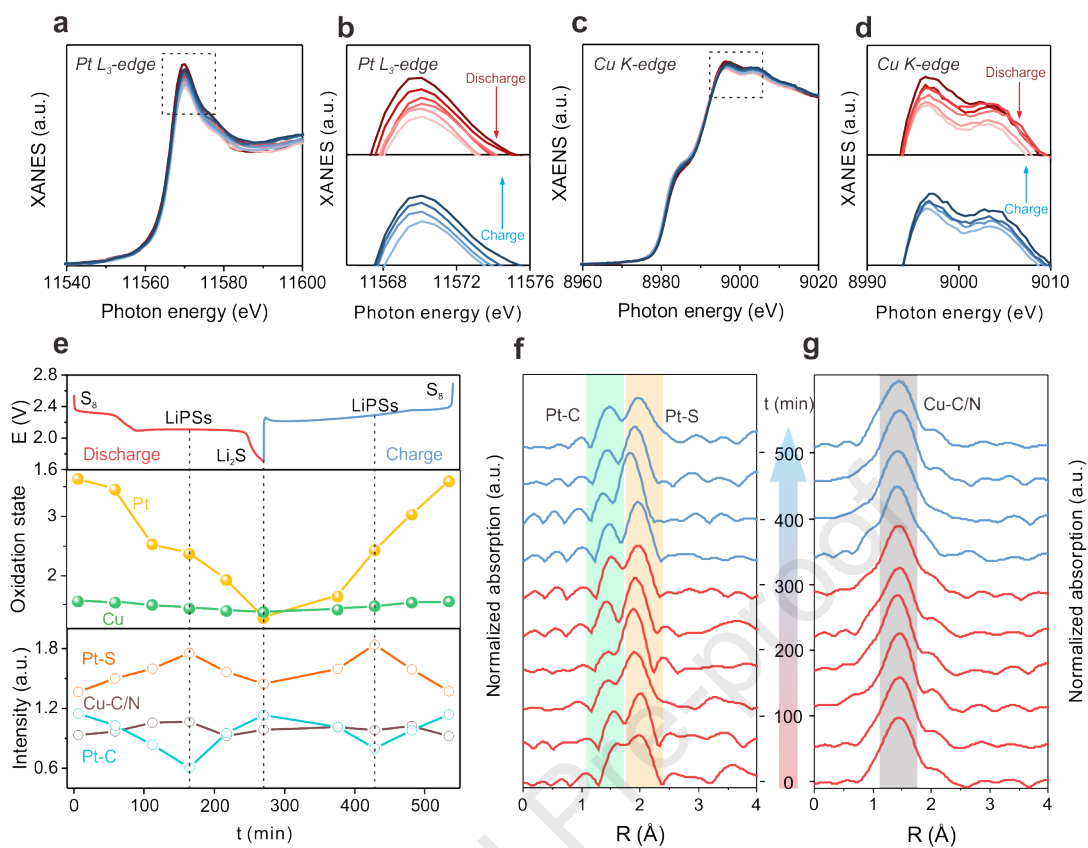
- 1 [33] S. Feng, Z.-H. Fu, X. Chen, B.-Q. Li, H.-J. Peng, N. Yao, X. Shen, L. Yu, Y.-C.  
2 Gao, R. Zhang, Q. Zhang, An electrocatalytic model of the sulfur reduction reaction in  
3 lithium-sulfur batteries, *Angew. Chem. Int. Ed.* 61 (2022) e202211448.
- 4 [34] G. Zhou, S. Zhao, T. Wang, S.-Z. Yang, B. Johannessen, H. Chen, C. Liu, Y. Ye, Y.  
5 Wu, Y. Peng, C. Liu, S. P. Jiang, Q. Zhang, Y. Cui, Theoretical calculation guided design  
6 of single-atom catalysts toward fast kinetic and long-life Li-S batteries, *Nano Lett.* 20  
7 (2020) 1252-1261.
- 8 [35] Z. Han, S. Zhao, J. Xiao, X. Zhong, J. Sheng, W. Lv, Q. Zhang, G. Zhou, H.-M.  
9 Cheng, Engineering d-p orbital hybridization in single-atom metal-embedded three-  
10 dimensional electrodes for Li-S batteries, *Adv. Mater.* 33 (2021) 2105947.
- 11 [36] Z. Zeng, W. Nong, Y. Li, C. Wang, Universal-descriptors-guided design of single  
12 atom catalysts toward oxidation of  $\text{Li}_2\text{S}$  in lithium-sulfur batteries, *Adv. Sci.* 8 (2021)  
13 2102809.

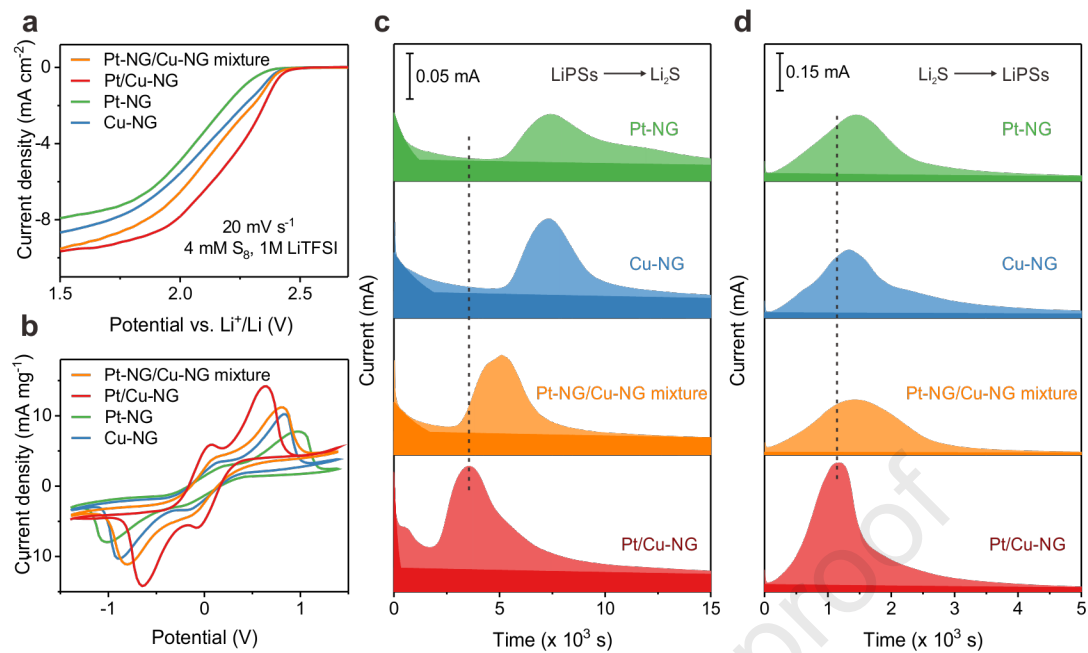
#### 14 Graphical Abstract

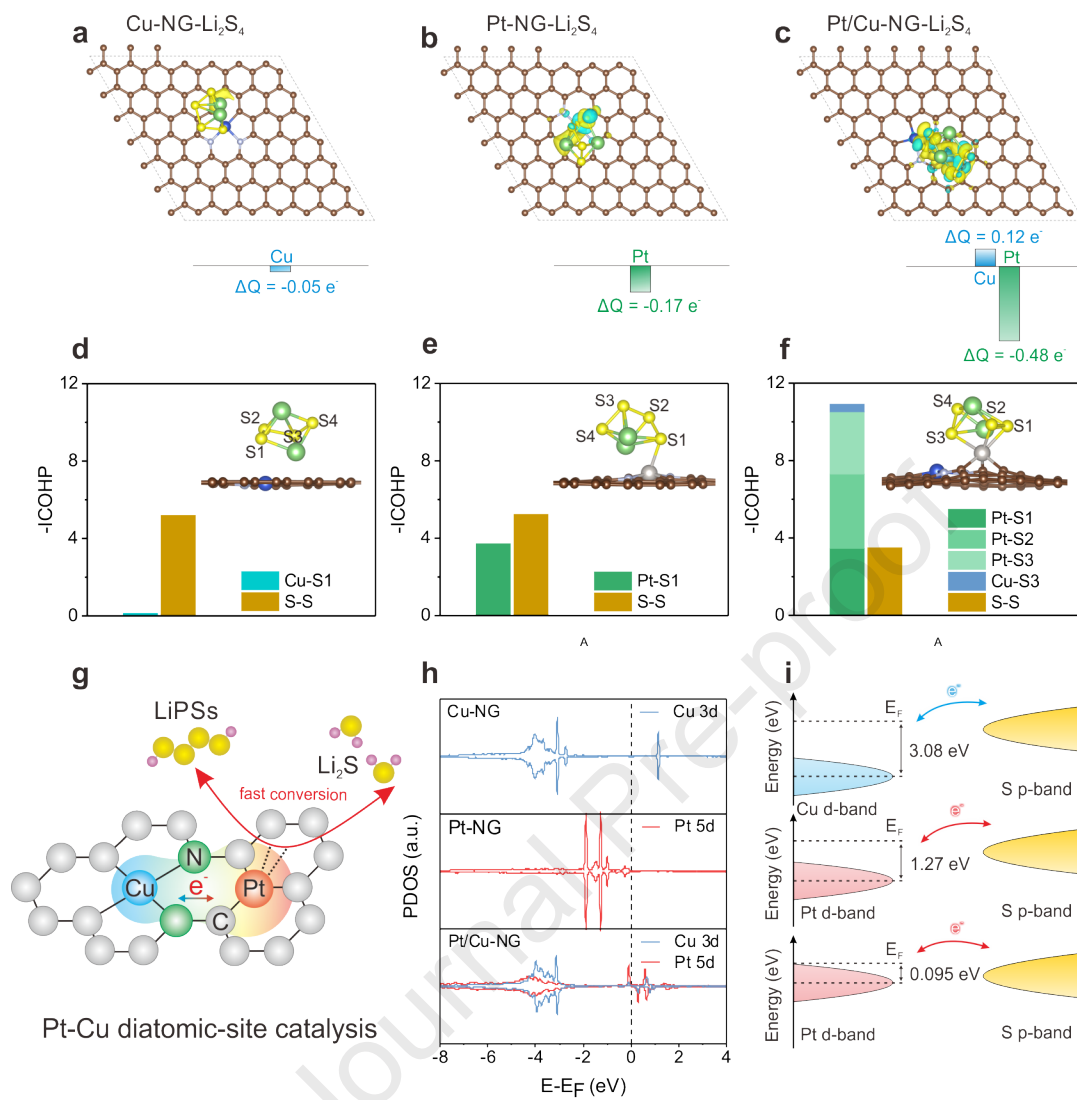


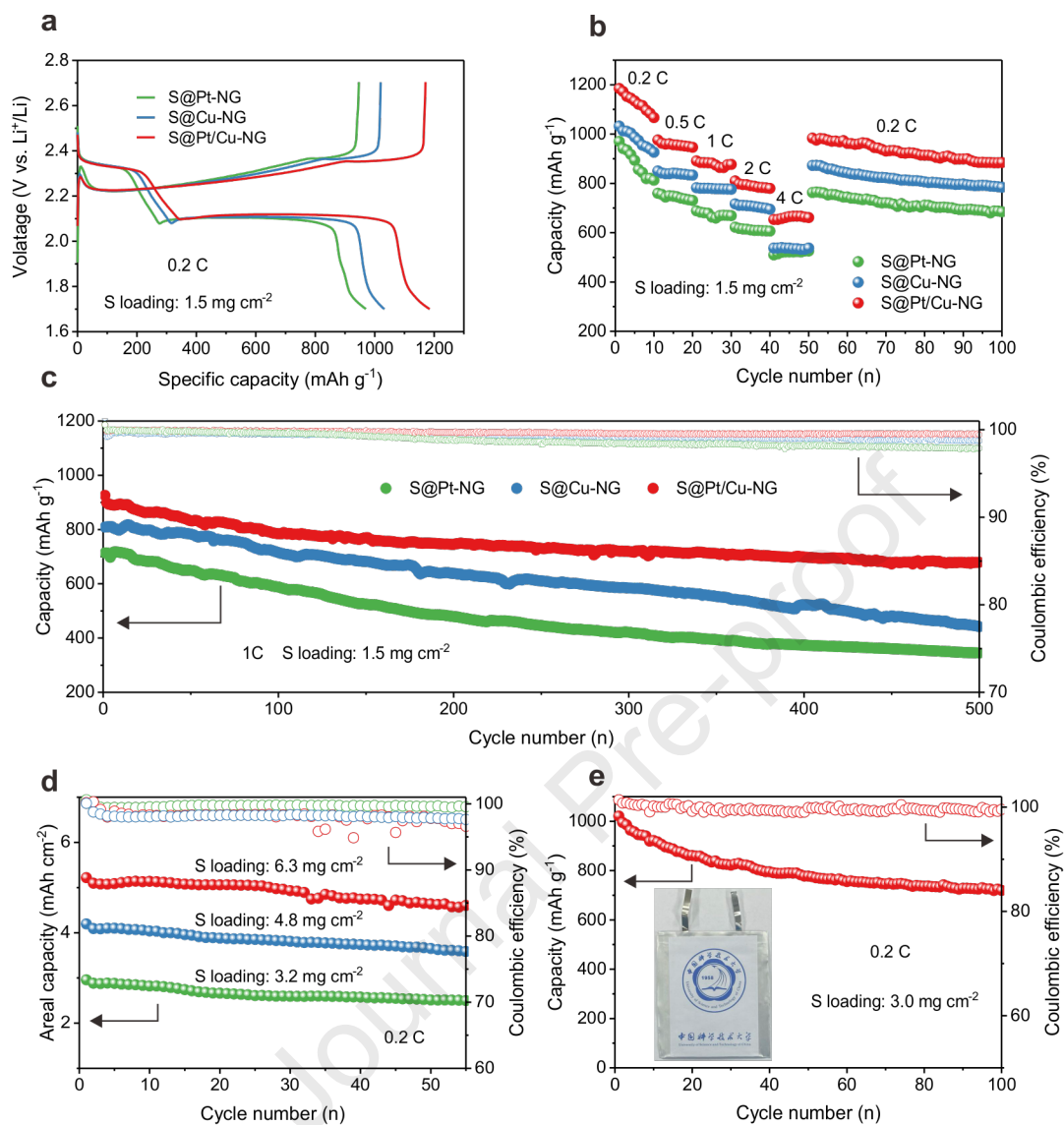






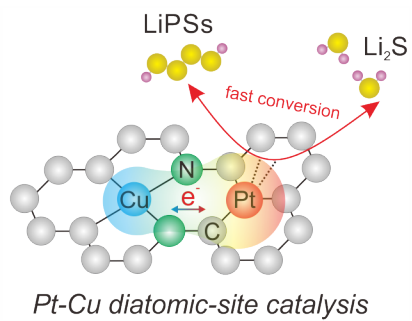






**Highlights**

- Pt-Cu dual-atomic sites boost sulfur redox reaction kinetics for Li-S batteries.
- *Operando* X-ray absorption spectroscopy (XAS) and density functional theory (DFT) calculations reveal the synergistic effects operative in DACs on the atomic scale.
- A synergistic effect between the paired Pt and Cu atoms modifies the electronic structure of the Pt site through d-orbital interactions.



Journal Pre-proof

**Declaration of interests**

The authors declare that they have no known competing financial interests or personal relationships that could have appeared to influence the work reported in this paper.

The authors declare the following financial interests/personal relationships which may be considered as potential competing interests:

Journal Pre-proof